A physics-based atmospheric and BRDF correction for Landsat data over mountainous terrain

Fuqin Li [a,*], David L.B. Jupp [b], Medhavy Thankappan [a], Leo Lymburner [a], Norman Mueller [a], Adam Lewis [a], Alex Held [b]

[a] National Earth Observation Group, Geoscience Australia, GPO Box 378, ACT, 2601, Australia
[b] CSIRO, Marine and Atmospheric Research, GPO Box 3023, ACT 2601, Australia

ARTICLE INFO

ABSTRACT

Steep terrain affects optical satellite images through variations it creates in both irradiance and bidirectional reflectance distribution function (BRDF) effects. To obtain the corrected land surface reflectance and detect land surface change through time series analysis over rugged surfaces, it is necessary to remove or reduce the topographic effects. In this paper a physics-based BRDF and atmospheric correction model that handles both flat and inclined surfaces in conjunction with a 1-second SRTM (Shuttle Radar Topographic Mission) derived Digital Surface Model (DSM) product was applied to 8 Landsat scenes covering different seasons and terrain types in eastern Australia. Visual assessment showed that the algorithm removed much of the topographic effect and detected deep shadows in all 8 images. An indirect validation based on the change in correlation between the data and terrain slope showed that the correlation coefficient between the surface reflectance factor and the cosine of the incident (sun) angle reduced dramatically after the topographic correction algorithm was applied. The correlation coefficient typically reduced from 0.80–0.70 to 0.05 in areas of significant relief. It was also shown how the terrain corrected surface reflectance can provide suitable input data for multi-temporal land cover classification in areas of high relief based on spectral signatures and spectral albedo, while the products based only on BRDF and atmospheric correction cannot. To provide comparison with previous work and to validate the proposed algorithm, two empirical methods based on the C-correction were used as well as the established SCS-method to provide benchmarks. The proposed method was found to achieve the same measures of shade reduction without empirical regression.

Crown Copyright © 2012 Published by Elsevier Inc. All rights reserved.

1. Introduction

Topographic correction of satellite images over mountainous or hilly areas is very important (Liang, 2004), especially when the data are to be used for land cover mapping and monitoring over time. Steep terrain affects optical satellite images through both irradiance and Bi-directional Reflectance Distribution Function (BRDF) effects (Dymond et al., 2001; Gu & Gillespie, 1998). Slopes facing toward the sun receive more solar irradiance and appear brighter in satellite images than those facing away from the sun (Iqbal, 1983, Chapters 10, 11) where the darker pixels are often said to be "shaded". In addition, for anisotropic surfaces, the radiance received at the satellite from inclined surfaces is also affected by surface BRDF. That is, the signal results from the combined effects of surface land cover structure interacting with the sun and satellite geometry (sun and view and

its relative azimuth angle) as well as topographic geometry (e.g. slope and aspect angles). Finally, all of these factors affect the inversion of land surface parameters and applications that aim to detect land surface conditions and changes through time series analysis.

Following some years of development and improvement, physics-based models for BRDF and atmospheric correction are relatively mature (Li & Strahler, 1985; Li et al., 1995; Li et al., 2010; Schaaf et al., 2002; Vermote et al., 1997). However, they have been applied mostly to surfaces that are essentially flat and seldom to significantly inclined surfaces. In the past, reported Digital Surface Model (DSM) or Digital Elevation Model (DEM) based topographic correction has mostly been undertaken separately from BRDF and atmospheric correction. Typical examples are terrain illumination correction for Lambertian surfaces (Dozier & Frew, 1981, 1990) and the "C-correction" (cosine) method which is based on an empirical relationship between observed radiance from inclined surfaces and the cosine of the incident angle (Richter, 1997; Teillet et al., 1982). Gu and Gillespie (1998) proposed the Sun-Canopy-Sensor (SCS) topographic correction which accounts for some of the BRDF effects over forested mountain areas and Shepherd

and Dymond (2003) developed a semi-physics-based terrain and BRDF model which assumed an empirical relationship between diffuse reflectance and direct reflectance and other assumptions.

In this paper, a complete physics-based coupled BRDF and atmospheric model for both horizontal and inclined surfaces is introduced. The model unifies atmospheric, BRDF and topographic correction, extending work reported by Li et al. (2010) to include varying terrain within the same operational framework. It is important to specify that the work described is to be applied at the spatial resolution of Landsat, SPOT and similar resolution satellites. The correction assumes that the hill slopes are resolved by the sensor system. For satellites with large Instantaneous Field Of View (IFOV), such as MODIS 1 km data, the terrain effect is better treated as a modification to the BRDF, such as in the Hapke (1981) model. Two areas of Australia with significant terrain effects were selected to test the model and the model performance and make a comparison with other typical topographic correction methods.

The method, its relationship with other commonly used topographic correction methods and some implementation issues are described in Section 2 and Appendix A which provides greater detail for the mathematics. The information collected and materials used to validate the basic method are described in Section 3. Section 4 provides the results of three kinds of validation; visual, de-correlation with incident angle and land cover effects. Section 5 discusses some specific aspects arising from the results and the paper is concluded in Section 6.

2. Methods selected for the study

2.1. Basic approach

The base method introduced in this paper combines physical modelling with atmospheric, BRDF and terrain correction of the data. The approach seeks to avoid empirical or image dependent methods as much as possible and allow automation of products. The atmospheric and BRDF correction approaches have been described and validated in Li et al. (2010) and a number of issues relating specifically to the terrain information are discussed in Li et al. (2011). This paper extends the methods described by Li et al. (2010) to account for shading variations observed in areas with significant terrain complexity.

For flat terrain, as described in Hu et al. (1999), Vermote et al. (1997) and Li et al. (2010), radiance received by satellite sensors for non-uniform surfaces can be expressed as:

$$
L_{\text{TOA}} = L_0 + \frac{1}{\pi} E'_0 \cos(\theta_{\text{S}})
\begin{pmatrix}
t_{\text{V}} t_{\text{S}} \rho_{\text{S}}(\theta_{\text{S}}, \theta_{\text{V}}, \delta\varphi) + t_{\text{V}} t_{\text{d}}(\theta_{\text{S}})\overline{\rho} + t_{\text{S}} t_{\text{d}}(\theta_{\text{V}})\overline{\rho'} + \\
t_{\text{d}}(\theta_{\text{S}}) t_{\text{d}}(\theta_{\text{V}})\overline{\rho} + \dfrac{[t_{\text{V}} + t_{\text{d}}(\theta_{\text{V}})][t_{\text{S}} + t_{\text{d}}(\theta_{\text{S}})]S\left(\overline{\overline{\rho}}\right)^2}{1 - S\overline{\overline{\rho}}}
\end{pmatrix}
$$

(1)

In this equation, $\delta\varphi$ is the relative azimuth between the sun and view directions, $\overline{\rho}, \overline{\rho'}$ and $\overline{\overline{\rho}}$ are surface hemispherical–directional, directional–hemispherical and hemispherical–hemispherical reflectance (or bi-hemispherical) factors, respectively, other terms are defined in Table 1.

When the land surface is Lambertian (uniform bi-directional reflectance factor, or BRF, in all directions and denoted ρ_{m}) the model simplifies allowing a straightforward solution as:

$$
\frac{\rho_{\text{m}}}{1 - S\rho_{\text{m}}} = \frac{\pi(L_{\text{TOA}} - L_0)}{E_{\text{h}} T_{\text{V}}}
$$

(2)

Symbols are defined in Table 1. In the general case, the first four of five terms inside the brackets of Eq. (1) enable the atmospheric

Table 1
Main symbols used in the paper.

θ_{S}	solar zenith angle
φ_{S}	solar azimuth angle
θ_{V}	sensor view zenith angle
φ_{V}	sensor view azimuth angle
θ_{t}	slope angle
φ_{t}	aspect angle of the slope
i_{t}	incident zenith angles between the sun and view directions and surface normal
φ_{i}	azimuth angle for incident direction in the slope geometry
e_{t}	exiting zenith angles between the sun and view directions and surface normal.
φ_{e}	azimuth angle for exiting direction in the slope geometry
t_{S}	direct transmittance in the solar direction
t_{V}	direct transmittance in the view direction
$t_{\text{d}}(\theta_{\text{S}})$	diffuse transmittance in the solar direction
$t_{\text{d}}(\theta_{\text{V}})$	diffuse transmittance in the view direction
S	the atmospheric albedo
T_{S}	total transmittance in the solar direction
T_{V}	total transmittance in the view direction
L_{TOA}	Sensor radiance at top of atmosphere
L_0	path radiance
E'_0	Solar exoatmospheric irradiance (earth-sun distance adjusted).
ρ_{S}	the surface reflectance (the BRF or bi-directional reflectance factor which is π times the BRDF)
ρ_{adj}	average reflectance of adjacent objects
ρ_{m}	the atmospherically corrected Lambertian reflectance
E_{h}	total irradiance on a horizontal surface
$E_{\text{h}}^{\text{dir}}$	the direct component of irradiance on a horizontal surface
$E_{\text{h}}^{\text{dif}}$	the diffuse component of irradiance on a horizontal surface
E	total irradiance on an inclined surface
E^{dir}	direct component of irradiance on an inclined surface
E^{dif}	diffuse component of irradiance on an inclined surface

correction methodology to be extended to include non-Lambertian surfaces. The fifth term allows for the interaction between the surface and atmosphere. It is shown in Appendix A that a solution is possible if the "shape function" for the BRDF is known and Appendix A contains details of the solution as well as equations that extend it to include terrain shading effects.

When there is terrain variation in an area, the primary modification to the equation occurs because the diffuse and direct components of the total irradiance are modified. Assuming that the pixels are part of an inclined slope facet and that the modification to the diffuse and direct irradiance is as described by Iqbal (1983), the effects can then be incorporated into the four terms in Eq. (1) to take account of the modified irradiances. Appendix A also shows how BRDF is included by modifying the sun and view angles on the surface. The modified angles needed to describe solar radiation transfer for horizontal and inclined surfaces are illustrated in Fig. 1.

For both irradiance and BRDF modification, the sun and view angles are transformed into new angles relative to the slope normal rather than measured relative to the gravity normal. In particular, if the sun zenith and sun azimuth are denoted as $(\theta_{\text{S}}, \varphi_{\text{S}})$, the view zenith and view azimuth as $(\theta_{\text{V}}, \varphi_{\text{V}})$ and the slope facet zenith and slope azimuth as $(\theta_{\text{t}}, \varphi_{\text{t}})$ then equivalent incident $(i_{\text{t}}, \varphi_{\text{i}})$ and exiting $(e_{\text{t}}, \varphi_{\text{e}})$ angles can be defined for the new coordinate system. For Lambertian surfaces, only the incident zenith angle is needed to define the configuration factor and it is:

$$
\cos(i_{\text{t}}) = \cos(\theta_{\text{S}})\cos(\theta_{\text{t}}) + \sin(\theta_{\text{S}})\sin(\theta_{\text{t}})\cos(\varphi_{\text{S}} - \varphi_{\text{t}})
$$

(3)

A mathematical description of the terrain is needed to implement the model, which is best provided by a DSM. The DSM allows the slope and aspect to be defined at any point and consequently the computation of the transformed angles and other information. The detailed expressions and solutions involving the interaction of BRDF terms and these components are given in Appendix A. The main assumption is
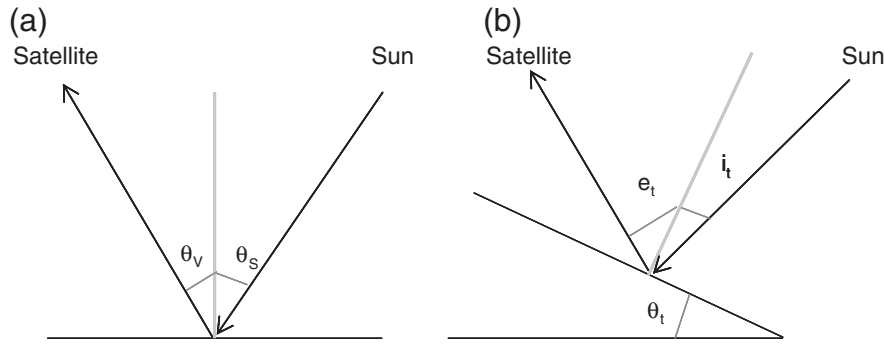
Fig. 1. Schematic diagram for solar radiation transfer: (a) horizontal surface and (b) inclined surface.

that the BRDF expressions are those used for the flat surfaces but evaluated using the projected incident and exiting angles. This assumption will be discussed later. Fig. 2 presents the complete algorithm as a flow chart. The top three lines of the flow chart address the atmospheric correction and angle calculations as well as the deep shadow detection algorithm which are needed by all terrain correction methods. The bottom box addresses the proposed topographic correction method of this paper and its key equations.

2.2. Other commonly used topographic correction methods

The relationship between the physics-based method described in this paper and others in common use can be clarified by considering the terrain based solution in the case when the surface is Lambertian. In this case, using definitions from Table 1 and Equations from Appendix A, the ratio of total irradiance onto sloping terrain (E) to total irradiance on a horizontal surface (E_h) can be written as:

$$R = \frac{E}{E_h} = f_S \frac{\cos(i_t)}{\cos(\theta_S)} + (1 - f_S)F_d + F_t \rho_{adj} \tag{4}$$

The view factors for diffuse radiation (F_d) and nearby terrain (F_t) are given in Appendix A and $f_S = t_S/T_S$. By making appropriate substitutions into the equations in Appendix A the solution becomes:

$$\rho_{lt} = \frac{\rho_m}{R + (1 - R)S\rho_m} \tag{5}$$

ρ_{lt} can be regarded as a terrain (irradiance) corrected Lambertian surface reflectance factor.

In cases where there is no diffuse radiation (f_S is close to one) with negligible radiation scattered from the surrounding terrain and atmosphere, and assuming no cast shadow areas (sun not too low) this simplifies to:

$$\rho_{lt} \approx \rho_m \frac{\cos(\theta_S)}{\cos(i_t)} \tag{6}$$

This expression (the simple cosine correction) is well-known and discussed in a number of papers for terrain shading effects such as Soenen et al. (2005) and Richter et al. (2009). Most writers report that the simple cosine correction is not a good way to correct the
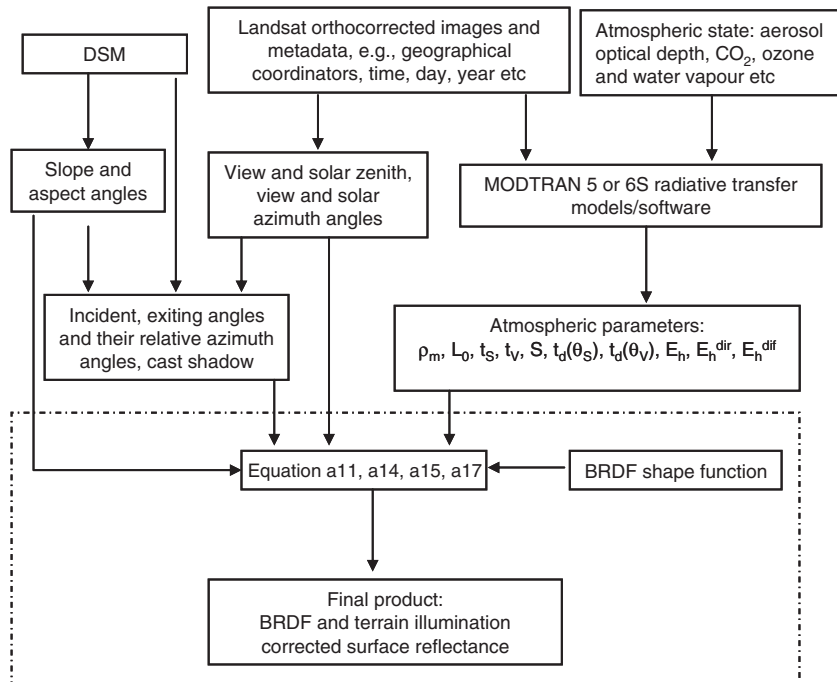

Fig. 2. Flow chart for the algorithm.

data and attribute part of its poor performance to the fact that diffuse radiation has not been taken into account (Teillet et al., 1982). To overcome this limitation, Teillet et al. (1982) introduced the C-Correction (CC) method. In this method, a regression is obtained between $\cos(i_t)$ and ρ_m using an area of the image that has significant terrain and is representative. This can be written as:

$$\rho_m \approx a \cos(i_t) + b \qquad (7)$$

Teillet et al. (1982) then proposed a correction (writing C for b/a and denoting the method the "CC" method):

$$\rho_{CC} = \rho_m \frac{\cos(\theta_S) + C}{\cos(i_t) + C} \qquad (8)$$

This has been shown in almost all cases to provide a better behaved correction for terrain than the cosine method (Soenen et al., 2005; Wu et al., 2004). Many people have used this approach. Wu et al. (2004) describe its successful use in an operational setting. However, they have also documented the difficulties faced when a method is data dependent and empirical. The regression must be repeated for each image data set, representative locations are often hard to find and it is time consuming and expensive to implement. In some situations, when there is extensive cloud cover, it is hard to estimate an effective value for C to use in Eq. (8). There is also no BRDF correction in the method which can lead to significant error in time series analysis.

Gu and Gillespie (1998) described a method that does not use empirical regression and also takes some account of BRDF effects in mountain forests. It is called the "SCS" method for "Sun-Canopy-Sensor". Gu and Gillespie's method can be expressed as:

$$\rho_{scs} = \rho_m \frac{\cos(\theta_t) \cos(\theta_S)}{\cos(i_t)} \qquad (9)$$

The term $\cos(\theta_t)$ is added to make allowance for change in shadow with slope angle in structured canopies on slopes. Soenen et al. (2005) combined the approaches with their "SCS + C" method which tends to behave in a very similar way to the CC method above. An empirically calibrated Minnaert model (Richter, 1997; Smith et al., 1980) has also been used to take account of terrain effects.

In this paper, only the CC, SCS and SCS + C approaches will be used to compare with the proposed physics-based model. The Minnaert, SCS and CC methods have all been shown to provide better results than the simple cosine ratio correction and the Minnaert and CC methods are generally similar in previous comparisons (e.g. Richter et al., 2009). The semi-physics based method described by Shepherd and Dymond (2003) will also be taken to be similar to the method described in this paper and not included in the comparison. Any differences are more appropriately discussed in another context.

2.3. Implementation issues

2.3.1. DSM model and derivation of terrain parameters

The implementation of the combined atmospheric and BRDF correction has been discussed previously in Li et al. (2010). The primary new input to the terrain correction is a DSM. In this paper, the definitions of DSM and DEM follow those in documentation provided by Geoscience Australia and The Commonwealth Scientific and Industrial Research Organisation (CSIRO) Land and Water (2010). They are that DSMs provide surface height above sea level and may include trees and other rough features, whereas DEMs estimate the elevation of the soil surface free of fine scale roughness elements such as trees and buildings. The DSM is primarily used here to derive terrain parameters, such as slope angle, aspect angle and cast shadow.

When dealing with terrain illumination correction, the "deep shadow effect" (areas not accessed by direct sunlight) cannot be ignored.
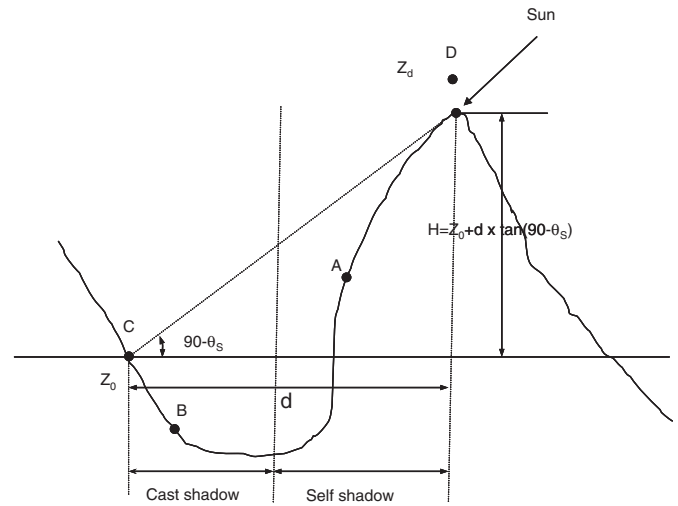

Fig. 3. Self shadow and cast shadow diagram for the sun direction.

There are two types of deep shadow (see Fig. 3), which will be referred to as self shadow and cast shadow. "Self shadow" is where direct radiation does not reach a pixel as the surface faces away from the sun (or view) direction and has sufficient slope so that it cannot be "seen" from either of these directions. It occurs when the incident angle $i_t \geq 90$ or exiting angle $e_t \geq 90$ (e.g., A in Fig. 3). "Cast shadow" refers to the situation where pixels are shadowed by adjacent terrain along the sun or view direction. It can occur even where the surface itself may face towards the light source but where another part of the surface blocks the light from reaching it, e.g., B in Fig. 3. Fig. 3 describes the geometry used for the cast and self shadow algorithms for the given sun direction. Self shadow can be calculated from slope and aspect. However, calculating cast shadow requires reference to the surrounding terrain out to a distance that depends on the sun elevation and is therefore more computationally intensive. The most popular algorithm is the horizon algorithm developed by Dozier et al. (1981) but it is computationally intensive.

In this study, a simpler and faster cast shadow algorithm is used based on the algorithm described by Giles (2001). Basically, from a given location at C (see Fig. 3) with elevation z_0, if the sun has solar zenith θ_S and solar azimuth angles φ_S, the location is "visible" if the ray from the location to the sun does not "hit" the terrain, and it is in "cast shadow" or occluded if the line intersects the terrain (Fig. 3). At location C, if some place in the direction of the sun, for example D, is such that the elevation of $Z_d \geq h = Z_0 + d \times \tan(90 - \theta_S)$, then C is occluded by D. Using these algorithms, the terrain information as well as the locations of self and cast shadow were obtained from the DSM. In our work, if a pixel is in deep shadow it is masked out as Landsat does not have the dynamic range to estimate reflectance in deep shadow areas. In the following sections, areas that receive no direct sunlight as a result of self shadowing or cast shadows are referred to as "deep shadow", whereas areas illuminated at varying angles to the slope normal are referred to in terms of "terrain shading" to distinguish them from deep shadows. Deep shadow detection is needed for all the topographic correction methods, including the physics-based model proposed in this paper and the other commonly used methods (CC, SCS and SCS + C).

2.3.2. BRDF model

The previous implementation of the BRDF effect (Li et al., 2010) in a physics-based model used the MODIS BRDF product and ancillary information (such as black sky and white sky albedo) provided by the MODIS team. The BRDF model used in the terrain based algorithm is again the Ross thick for volume and Li sparse for geometry (Schaaf et al., 2002). This is the reciprocal form of the model and is used by the MODIS group for their operational BRDF product. However,

since the MODIS sensor view zenith angle is no greater than 60° and the range of sun angles over the compositing period is also well within this range, the MODIS BRDF data are estimated from data within a limited range. In high relief areas, projected incident and exiting angles are often in excess of 60° which can cause the kernel model to be unstable as it is going beyond its data limits and also probably beyond its limits as an approximation to the original BRDF models. In the implementation described here, the stability has been modified by selecting a threshold angle beyond which the incident and exiting angles are not allowed to go.

Fig. 4 plots BRDF shape (from the Nov. 9, 2009 data) changes with view/or solar zenith angle for the principal and cross principal plane. In the figure, the solar angle is fixed as 30°, 45°, 60° and 75°, respectively for Fig. 4a, b, c and d. The results show that when the solar zenith angle is fixed at 30°, the BRDF model is stable until a view zenith angle of 88° is reached. When the solar zenith angle increases, the threshold for the view zenith angle before BRDF is unstable becomes smaller. When the solar zenith angle is 75°, BRDF becomes unstable when the view angle reaches 60°. Since the Ross–Li model is a reciprocal model, the results are the same for the solar zenith angle case when view angle is fixed. For this reason, when the reciprocal Ross–Li model is applied, the incident angle has been limited to 70° and exiting angle to 60° for the present implementation of the algorithm. In addition to the BRDF shape function, the polynomial formula for black sky albedo (Lucht et al., 2000) is also limited to an angle range between −80° and 80°. It seems, therefore, that when both incident and exiting angles go beyond 80°, the black sky albedo can also become unstable. In the proposed algorithm, the threshold for both

incident and exiting angles has been set to 80° for the black sky albedo calculation.

For many surfaces, such as snow, compact soil, rock and short vegetation, the assumption that the BRDF effect for the slope is the BRDF for the rotated angles should represent the slope effect well. For tree canopies, as explained in Dymond et al. (2001) and Gu and Gillespie (1998), there will be geometric effects that depend on how close to the gravity normal the tree stems grow and (for broad leaf vegetation) the fact that leaves will orient relative to the gravity rather than slope normal. Dymond et al. (2001) modified a forest BRDF model to handle this, but since a wide range of possible land covers must be handled, it has been assumed that they are second order effects compared with the primary rotation into the coordinate system of the slope and a uniform correction has been applied. In support of this choice, Schaaf et al. (1994) investigated the effect of terrain on the Li–Strahler model (on which the Li-sparse kernel was based) and found the need to undergo two angle transformations. However, as the MODIS Li-sparse model assumes spherical crowns it results in what has been assumed here.

2.3.3. Instability in areas of low signal

As described above, the ratio of direct irradiance on a sloping surface to the direct irradiance on a horizontal surface is $\cos(i_t)/\cos(\theta_s)$. In the special case of Lambertian surfaces and no diffuse radiation, the limit of the current method is basically the simple cosine correction (see Eq. 6). It can lead to overestimation of the reflectance factor for bands with small diffuse radiation on the slopes away from the sun with large incident angle, such as for Landsat bands 4, 5 and 7.
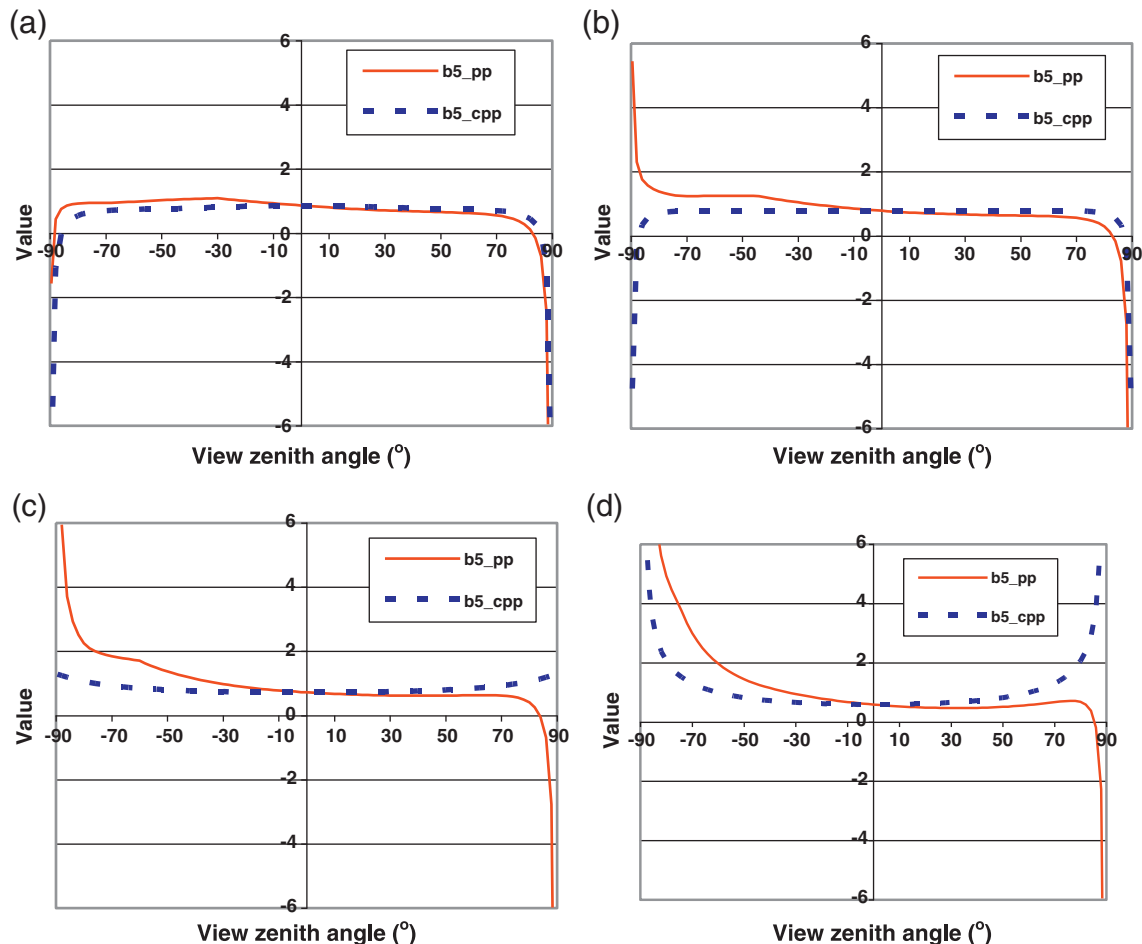

Fig. 4. BRDF shape changes with view angle using November 11, 2009 as an example. (a) at 30° solar zenith angle; (b) at 45° solar zenith angle (c) at 60° solar zenith angle and (d) at 75° solar zenith angle.

On slopes away from the sun at large incident angles the image data will have low intensity and the correction ratio will become large. At some point, the limited signal to noise ratio of the sensor system combined with low environmental signal to noise ratio will lead to the occurrence of unstable values (appearing over-corrected in the product). Places where the DSM curvature is high (such as across ridges) are particularly susceptible to this effect. Low signal areas will also be more common (for example) in winter and a strategy has been developed to handle them. This strategy involves modifying the direct radiation component (Eq. a11) according to:

$$\begin{cases} E^{dir} = E_h^{dir}\Theta\dfrac{\cos(i_t)}{\cos(\theta_S)} & \text{when } i_t < \beta \\[2mm] E^{dir} = E_h^{dir}\Theta\dfrac{\cos(i_t) + \cos(\alpha)}{\cos(\theta_S) + \cos(\alpha)} & \text{when } \beta \leq i_t < 90^o \text{ and } \alpha = 90 - i_t + \beta \\[2mm] E^{dir} = 0 & \text{when } i_t \geq 90 \end{cases}$$

$$(10)$$

where β is a threshold angle. In the present implementation of the algorithm, the limit is reached where R in Eq. (5) is less than 0.5, at which point the direct solar irradiance calculation is adjusted and the β is estimated through Eq. (5). With this modification, over-correction near ridges and other low illumination areas is reduced resulting in greater stability at the extremes. Further evaluation and monitoring may be needed to establish the most stable choice for this threshold.

3. Study areas and data description

3.1. Study areas

On the eastern margin of Australia, the topographic effect associated with the Great Dividing Range creates significant shading variation in remotely sensed data. Two areas were selected for this study to represent the variation in terrain and land cover commonly found in southeast Australia. These were the Australian Alps in the State of Victoria and the Blue Mountains in the adjacent State of New South Wales (NSW).

A relatively small (1000 by 1000 Landsat pixels) subset was selected from the area of the Australian Alps. It is located in the northeast of Victoria in the Landsat WRS (Worldwide Reference System) path 91 and row 85. The Australian Alps has the most significant topographic effects found in Australia. Its elevation is also the highest, reaching 2100 m above sea level. Another small (1000 by 1000 pixels) subset to the south of the Blue Mountains was selected and it is located in the upper middle of Landsat WRS path 90, row 84. Fig. 5 shows the DSM data in the two areas on an overview of Australia map.

3.2. Landsat image selection and pre-processing

Four clear Landsat 5 images for each area with varying solar angles were obtained to test the algorithm. Detailed information regarding the eight Landsat scenes is listed in Table 2. The four images with different solar zenith angles for each site provide us with an opportunity to test how the algorithm behaves with the range of solar zenith angles that occur at different times of the year. The ancillary input data needed to run the algorithm included atmospheric water vapour, aerosol optical depth, BRDF parameters as well as the DSM. The DSM data were used for this algorithm because tree height is retained in DSM data which is appropriate for topographic irradiance correction. Atmospheric water vapour was derived from radiosonde data measured by the Australian Bureau of Meteorology. For the Australian Alps, water vapour data were obtained from data collected at the Wagga Wagga meteorological station (35.16°S and 147.46°E), located within the same Landsat scene. For the Blue Mountains area, no radiosonde data were available for locations within the same scene,
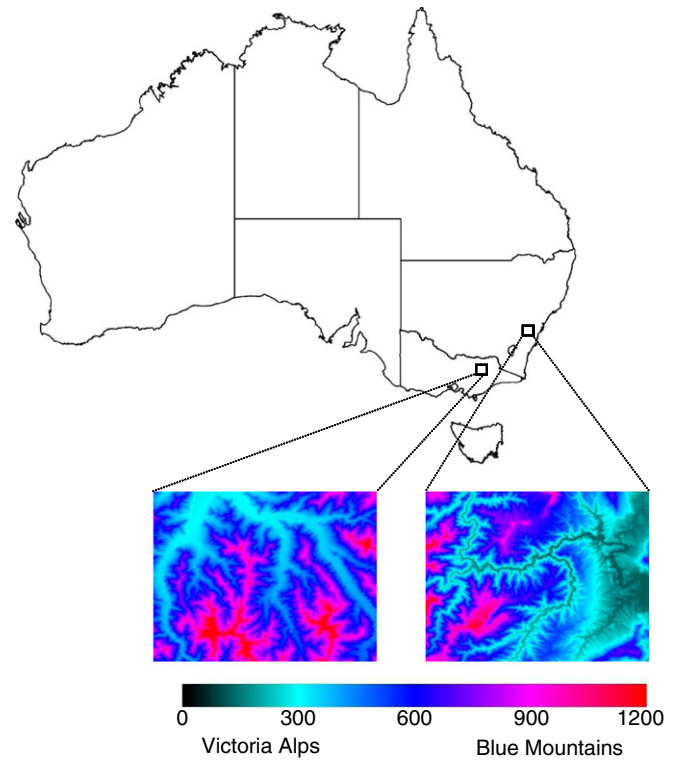

Fig. 5. DSM data (in meters) in the two study areas located on an Australian map.

therefore data from the nearest meteorological station (also Wagga Wagga) was used. The total precipitable water content comparison between the NOAA NCEP (National Centers for Environmental Prediction) reanalysis product (Kalnay et al., 1996) and Wagga Wagga radiosonde data showed that they were very close. The aerosol data were obtained from the local Aeronet station in Canberra (http://aeronet.gsfc.nasa.gov). The geographical location for this station is 35.271°S and 149.111°E and was appropriate for use in analysis of both images due to similarity of the atmospheric systems in the study sites.

BRDF parameters were obtained from the MODIS BRDF model product (Schaaf et al., 2002). Following Li et al. (2010), the BRDF shape is defined for large regions (regional scale); for this study, the average value over the Landsat scene extent was used but in the future this choice will be modified to one based on major land cover and terrain regions when the data are available. Landsat 5 images were provided by the National Earth Observation Group, Geoscience Australia. The Landsat images were ortho-corrected to equirectangular projection (latitude and longitude grid) as were also used in Li et al. (2010).

Table 2
Landsat 5 images used in the analysis.

Date (day/month/year)	Path	Row	Scene centre solar position	
			Solar zenith (°)	Solar azimuth (°)
06/01/2005	90	84	35.1	79.8
15/04/2006	90	84	55.41	43.01
21/08/2006	90	84	57.68	42.21
22/09/2006	90	84	46.02	48.13
08/03/2007	91	85	46.23	56.27
11/05/2007	91	85	62.69	36.46
25/02/2009	91	85	45.21	62.85
08/11/2009	91	85	34.03	64.11

3.3. Digital surface model (DSM) terrain information

Geoscience Australia and CSIRO have produced a 1-second Shuttle Radar Topography Mission (SRTM) derived DSM and DEM of Australia in February, 2010. The product includes a range of corrections for missing areas, striping and other SRTM artefacts (Geoscience Australia and CSIRO Land & Water, 2010). The DSM data needed to be further processed before being used for terrain correction. Various artefacts in the DSM data, which can have a significant effect on slope and aspect, needed be removed or reduced. For example, cases where the difference between a local median value and the corresponding central pixel exceed 20-30 metres occur in both DSM and DEM data at this scale. They create slope outliers. The data were also filtered using a Gaussian 3 by 3 filter to remove effects due to SRTM originally having a 1 metre vertical precision, and then resampled to Landsat resolution by the bilinear method. These and a range of other issues that arise in the use of DSM data in this context have been discussed in Li et al. (2011).

4. Results

4.1. Visual analysis

Four images from each selected area were processed using five different algorithms: (a) with atmospheric and BRDF correction only (Li et al., 2010), referred to as the standard corrected product in the following sections; (b) with atmospheric and BRDF correction plus topographic correction algorithm developed in this paper, referred to as the physics-based product in the following sections; (c) terrain corrected product from the CC method referred to as the CC product in the following sections; (d) terrain corrected product from the SCS method and referred to as the SCS product in the following sections and (e) terrain corrected product from the SCS + C method referred to as the SCS + C product in the following sections. When the coefficient C in Eq. (8) was derived, low relief areas in the Landsat images were masked out of the regression of Eq. (7) and for consistency, the composite deep shadow mask used with the physics-based product was also used with the CC, SCS and SCS + C methods. Three of the four images with solar zenith angles (θ_S) ranging from high, to moderate to low for each site are displayed in Figs. 6 and 7, respectively. Due to the similarity of the CC and SCS + C method, the SCS + C is not included in the visual assessment, but other comparisons are made in the later sections.

Fig. 6 shows the visual comparison between terrain corrected and standard corrected surface reflectance factors for the Australian Alps of Victoria. It is clear that the terrain shading at the hill slope scale has been reduced in the physics-based product (Fig. 6d, e and f), when compared with the standard corrected product (Fig. 6a, b and c). For example, the May 11, 2007 image (Fig. 6a, d) was collected near to the Australian winter and had a large solar zenith angle (64° in the area). The locations of deep shadow can be clearly seen in the standard corrected product (Fig. 6a), but were masked out in the physics-based terrain corrected images (Fig. 6d). The area of deep shadow decreases as the solar zenith angle decreases and there are fewer deep shadows in the November 11, 2009 image (Fig. 6f). Terrain shading is always present to some degree at finer (within-hill slope) scales and deep shadows are few to none in the summer but increase dramatically in the winter months.

The terrain shading is clearly significantly reduced in the physics-based product (Fig. 6d). The CC method is similar although Fig. 6i still shows some degree of terrain shading. It also seems some overcorrection has occurred in CC product (Fig. 6i). Overall, the CC method removes most of the terrain shading. However, the SCS method did not present good results. This last finding is consistent with those of Kane et al. (2008). The equivalent results in the Blue Mountains area are shown in Fig. 7. The images are in the

same sequence as in Fig. 6, that is, Fig. 7a had the largest solar zenith angle (closer to Australian winter) and the Fig. 7c has the lowest solar zenith angle (Australian summer). The results were similar to those obtained in the Australian Alps. The CC method seems to have achieved a better result but the SCS still appears the worst among the three methods.

Based on this visual assessment, it seems that the physics-based product and the CC method can reduce much of the topographic effect within the images from different seasons. However, while this kind of visual inspection has been used by others (e.g. Richter et al., 2009) it is not by itself sufficient to validate an operational product. Topographic correction is clearly difficult to validate using field reflectance measurements because it is hard to find a uniform target on an inclined surface which can be large enough to match the Landsat pixel resolution. It is even more difficult in rough terrain to obtain sufficient sample sites to carry out field validation. However, there are other indirect methods which can be used to indicate the degree of validity of the algorithm. One approach is to compute cross-plots between the cosine of the incident angle and computed reflectance factor (Wen et al., 2009) to measure the level of de-correlation achieved between them after correction. Another approach is to use land cover classification (Richter et al., 2009; Shepherd & Dymond, 2003; Wen et al., 2009).

4.2. De-correlation between irradiance and terrain

Due to the topographic effect, the surface reflectance on an inclined surface is strongly correlated with the cosine of the incident angle if no terrain illumination correction is made, but the reflectance factor should not generally be related to the cosine of the incident angle after the correction is applied. In the uncorrected data, the effect is most obvious in the data for band 4 since diffuse radiation in band 4 is very small and the signal/noise ratio is high. This band can therefore be used to test the level of de-correlation.

Table 3 lists the correlation coefficients between the $\cos(i_t)$ and band 4 reflectance factor for the selected scenes. The results from Table 3 show that the correlation coefficient between the $\cos(i_t)$ and the reflectance factor reduces dramatically after the terrain illumination correction is applied. For example, the correlation coefficient is reduced from 0.82 to 0.029 for August 21, 2006 and from 0.71 to 0.006 for March 8, 2007. Most of the absolute correlation coefficients for the eight scenes were below 0.1 after the terrain correction was applied, whereas most of them were above 0.5 before the correction was applied. The empirical CC and SCS + C achieved a high level of de-correlation for the eight scenes, especially the SCS + C method. However, the correlation coefficients are still high after SCS is applied. The performance by the empirical methods (CC and SCS + C) is to be expected as they are based on regression between the data and $\cos(i_t)$. However, the physics-based product obtained the same level of de-correlation without regression. This is a significant result.

4.3. Effects of terrain on land cover classification

Topography also affects the accuracy of land cover classifications and fractional vegetation cover products when they use brightness information and spectral signatures to derive land cover parameters. Even if the slopes facing towards and away from the sun have the same vegetation type, amount and condition, the spectral signatures will generally be different unless terrain illumination correction is applied. A reasonable expectation of terrain correction would be that the same land cover on sun facing and opposite slopes become similar in their signatures. Based on this expectation, an unsupervised classification approach has been used to establish how terrain correction can potentially improve the accuracy of land cover mapping based on spectral classification.
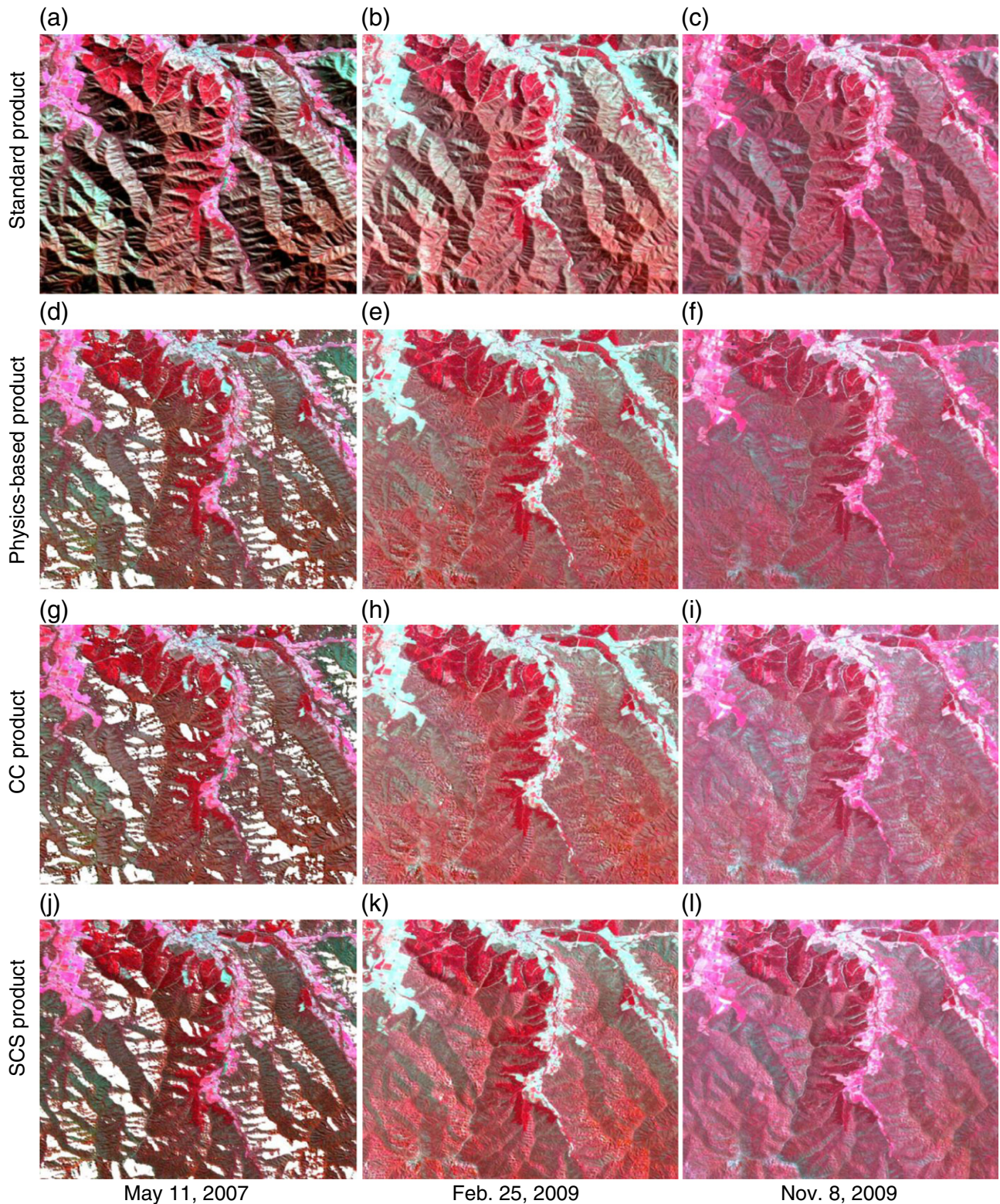
Fig. 6. False colour composite images of Australian Alps areas, Victoria (bands 4, 3, 2, white colour is detected as shadow). Three columns are for different dates, and four rows for different processing methodologies, respectively.

4.3.1. Development of the data set

A co-registered 1000 by 1000 subset was extracted from each of the four Landsat scenes in the Blue Mountains. The Blue Mountains area chosen is typical of the region and contains tablelands, steep ravines, deeply cut river valleys and high relief with inaccessible slopes covered by native vegetation. Temperate rain forest patches can be found in the gullies and the vegetation is very dense along the streams. Over the time sampled there were no changes to these land covers apart from normal response to environment and weather.

The number of pixels in deep shadow depends on the sun position and the terrain characteristics. For example, in the four images used here, one imaged on Aug. 21, 2006 had 6.41% of pixels in deep
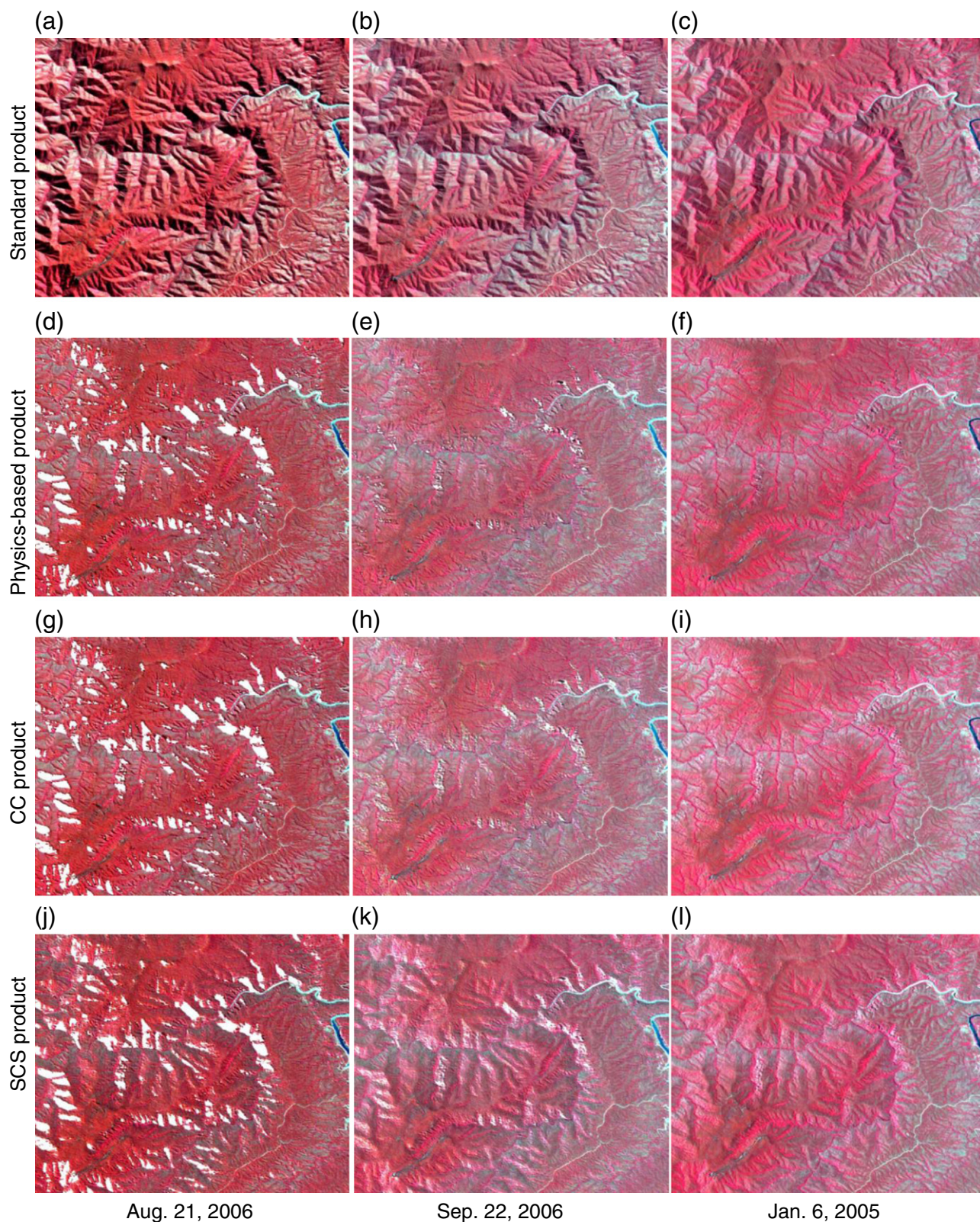
Fig. 7. False colour composite images of South Blue Mountains, NSW (bands 4, 3, 2, white colour is detected as shadow). Three columns are for different dates, and four rows for different processing methodologies, respectively.

shadow and another, imaged on Jan. 6, 2005 only had 0.12% of pixels in deep shadow. In order to develop common statistics for the areas, a composite mask for pixels that are in deep shadow in any of the four images was developed and these pixels were excluded from the comparison. Homogeneous land cover strata were produced for the

common area. Since the Normalized Difference Vegetation Index (NDVI) and other ratios are insensitive to terrain shading except in the darkest shadow areas (Kriegler et al., 1969; Wang et al., 1984), a multi-temporal 4-band image of the NDVI at each pixel for the four images was created in order that classes formed from it would

Table 3
Correlation coefficient between the cosine of the incident angle and Landsat band 4 reflectance factor in the selected targets and dates.

Date (day/ month/year)	Correlation coefficient				
	Before terrain correction	After terrain correction			
		Physics-based	CC	SCS	SCS + C
06/01/2005	0.5859	− 0.0723	− 0.1711	− 0.4650	− 0.0684
15/04/2006	0.8134	0.0485	− 0.0296	− 0.4954	− 0.0167
21/08/2006	0.8214	0.0290	0.0122	− 0.5187	0.0128
22/09/2006	0.7288	− 0.0920	− 0.1463	− 0.6400	− 0.0742
08/03/2007	0.7092	0.0058	0.0168	− 0.4201	0.0428
11/05/2007	0.6781	− 0.0613	0.1272	− 0.3968	0.1040
25/02/2009	0.8056	− 0.0156	− 0.0293	− 0.5636	0.0130
08/11/2009	0.4752	0.0946	0.0098	− 0.1734	0.0477

Table 4
Information about the land cover classes used.

Class number	Percent of image	Mean elevation (m)	Mean slope	Description
1 (Red)	16.65	544.8	19.91	Dense vegetation on top of escarpment
2 (Green)	53.57	463.59	17.70	Lower cover vegetation
3 (Dark blue)	20.56	354.81	19.50	Low cover vegetation and bright soil/rock
4 (Yellow)	1.67	244.07	12.60	Estuary banks
5 (Cyan)	1.07	118.19	0.24	Estuary

be as independent of terrain shading as possible and also sensitive to any areas that changed significantly. The composite image was classified into 20 classes using the ENVI K-Means method. The 20 classes were reduced by clustering to five major classes which were numbered in the order of decreasing average NDVI. The mean NDVI by image and class is as presented in Fig. 8.

Class 5 is a significant area of water and some adjacent land which is part of the Warragamba Dam (a deep flooded valley) and Class 4 is a mixed area adjacent to it which has considerable bare soil and rock cover. Classes 1, 2 and 3 are vegetation classes of varying cover and greenness with Class 1 having the highest NDVI and Class 3 the lowest in all four images. The small amount of change over time in these images provides us with a base of land covers that are persistent, having only changes in condition (such as summer stress) and almost certainly having no change in structure. A simple visual test of using Google Earth confirms these classes form three visually identifiable vegetation components in the area. Table 4 presents some additional information about the classes.

4.3.2. Separability of the classes in the primary data products

Statistics relating to the variously corrected Landsat images were generated using the class image as base. Table 5 summarises the variation among standard deviations within classes in two sub-tables. Table 5(a) summarises ratio of standard deviation between standard corrected product and terrain corrected product averaged over five classes for six bands and four dates. Large values indicate the much greater variance within the classes in the standard corrected product than in the terrain corrected product. The behaviour of the different bands is of special interest. Table 5(b) summarises the ratios of standard deviations for the standard corrected product with those of the physics-based terrain corrected
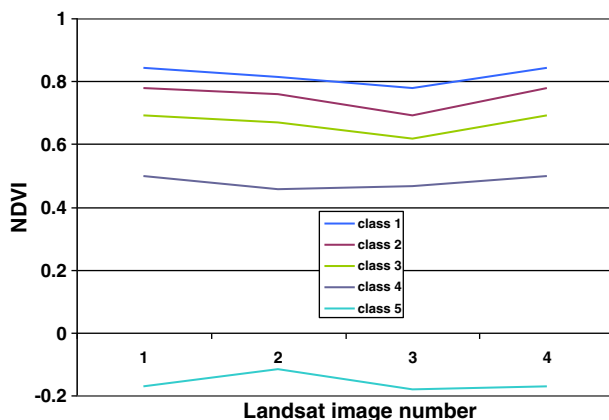
product averaged over six bands and presented for five class and four dates. Again, large values indicate the much greater variance within the class in the standard corrected product than in the terrain corrected product.

The behaviour of the different classes is of special interest in the second case. In the first 3 classes, the standard corrected images had a much greater within class variance than the terrain corrected data. The standard deviation data also indicate that the greatest additional within class standard deviation in the standard corrected product always occurs in Landsat Band 4 and was greatest in the winter image of Aug. 21, 2006. The greatest change in the mean due to the effects of terrain shading occurs for Class 3 and although there seems to be less in Classes 1 and 2 they are still much more variable due to terrain shading than Classes 4 and 5. It is reasonable to expect that Classes 4 and 5 show less change since they are relatively flat. Overall, the least differences are seen in all of the data from the summer image (06/01/2005) where the sun is highest. These are reasonable findings but more is needed.

For a more specific analysis of the spectral effects due to changes associated with the terrain effect and its various corrections, it is possible to separate the images into two sub-images. In one sub-image, the pixels were chosen so that the slope is greater than 15° and the aspect is to the North East (NE) or the azimuth to North ranges from 0° to 90°. In the other sub-image, the slopes are again defined to be greater than 15°, but the azimuths are to the South West (SW) or 180°–270° from North. These categories isolate parts of the image with an expected heightened brightness and those with expected lower brightness due to terrain shading. The Class image can also be separated in this way. Fig. 9 shows the classification presented in colour (colours listed in Table 4) with the two sub-images coloured by class in the same way but restricted to the two NE and

Fig. 8. Mean NDVI of five Land cover classes for four Landsat images of south Blue Mountains area where order of image numbers (from low to high) is Apr. 15, 2006, Aug. 21, 2006, Jan. 6, 2005 and Sep. 22, 2006.

Table 5
The ratio of standard deviations between standard corrected product and terrain corrected product, (a) average over classes and (b) average over bands.

(a)

Band	CWL[a]	Date (day/month/year)			
		15/04/2006	21/08/2006	06/01/2005	22/09/2006
1	478.71	1.12	1.12	1.07	1.07
2	561.04	1.15	1.14	1.10	1.08
3	661.44	1.15	1.14	1.07	1.09
4	834.57	1.38	1.38	1.21	1.26
5	1650.24	1.27	1.27	1.16	1.18
7	2208.12	1.18	1.18	1.10	1.12

(b)

Class	Date (day/month/year)			
	15/04/2006	21/08/2006	06/01/2005	22/09/2006
Class 1	1.49	1.51	1.31	1.40
Class 2	1.63	1.64	1.34	1.47
Class 3	1.70	1.71	1.36	1.47
Class 4	1.08	1.06	1.07	1.02
Class 5	1.00	1.00	1.01	1.00

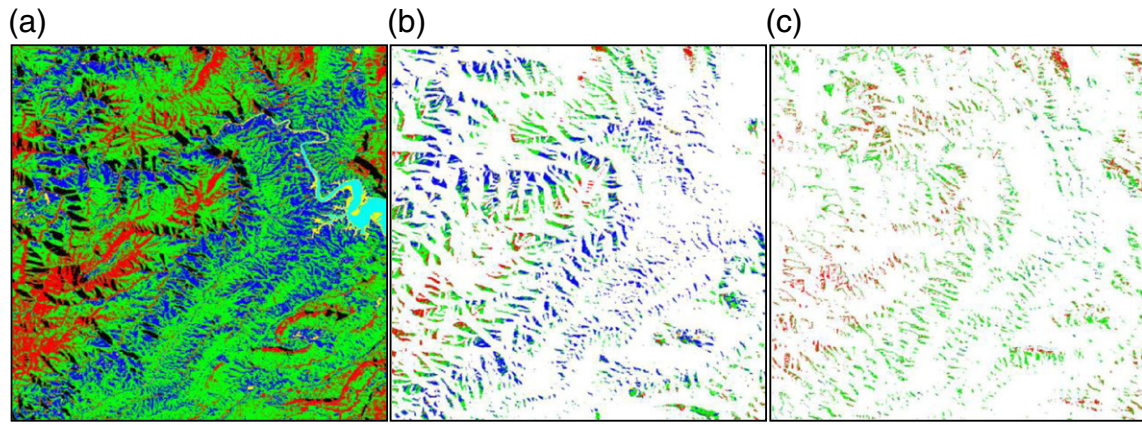[a] CWL is central wavelength for each band in nanometers.

Fig. 9. Classification image for south Blue Mountains, Class 1 is in red, Class 2 is in green, Class 3 is in dark blue, Class 4 is in yellow and Class 5 is in cyan, (a) Classification images for the whole area (shadows are masked as dark), (b) classification images for NE slopes (background and shadows are masked as white), and (c) classification images for SW slopes (background and shadows are masked as white).

SW "slope" classes. Class 3 is represented in blue and occurs dominantly on the NE slopes. Constructing these images allows comparisons between the mean signatures and standard deviations of the classes in the three cases of (i) all classified pixels not in deep shadow, (ii) only classified pixels in the NE slopes and (iii) only classified pixels in the SW slopes. For brevity, using the findings of Table 5, only the results for Classes 2 and 3 in the late autumn image of April 15, 2006 have been presented. These classes showed greatest overall variation in Table 5 and April 15, 2006 is a typical rather than an extreme example of the annual terrain shading variation.
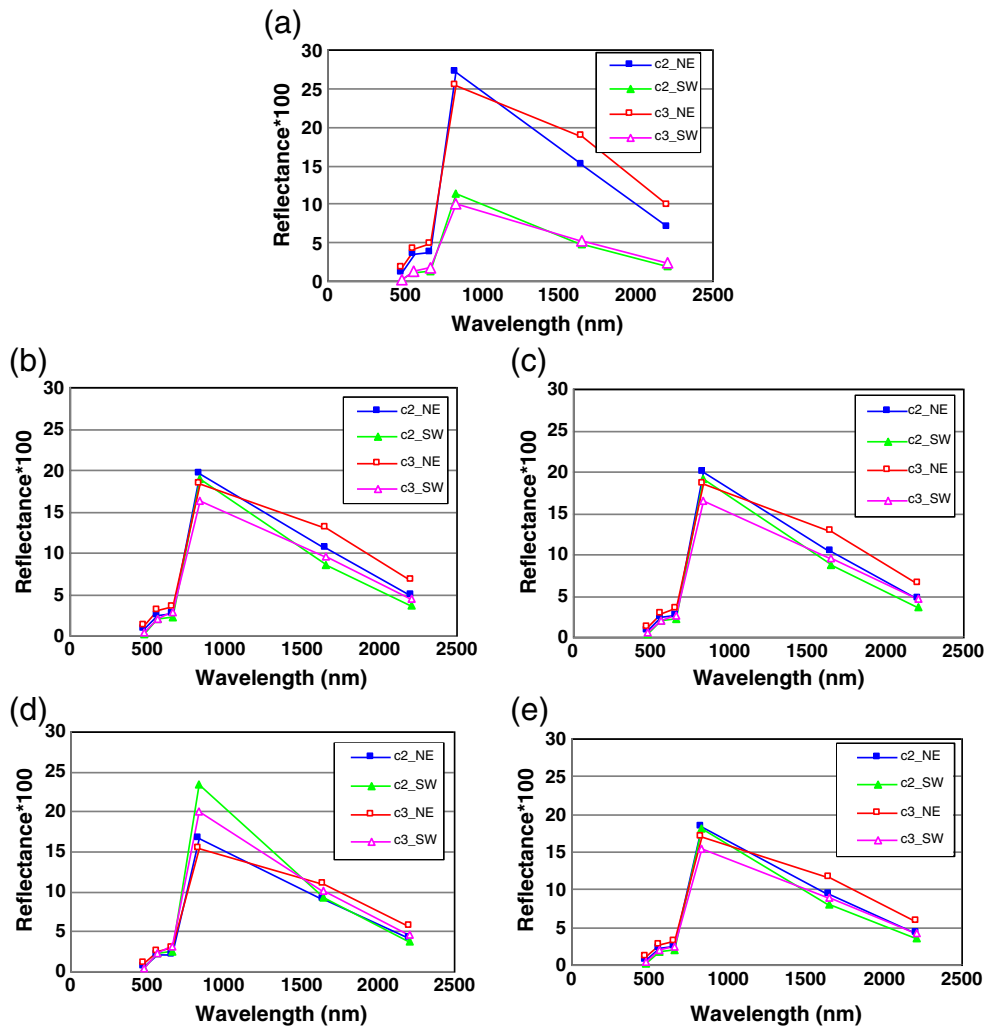

Fig. 10. Mean surface reflectance factors for Classes 2 and 3 for different slope strata, (a) standard product, (b) physics-based product, (c) CC product (d) SCS product and (e) SCS + C product. Where c2_NE is the mean surface reflectance factor for the NE slopes of Class 2, c2_SW is the mean surface reflectance factor for the SW of Class 2, c3_NE is the mean surface reflectance factor for the NE slopes of Class 3 and c3_SW is the mean surface reflectance factor for the SW of Class 3.

When the analysis is separated into the NE and SW slopes, the within-class variance (standard deviation) between the slope categories in the terrain corrected image (physics-based product) is generally small and would not disturb a classification in which the classes are used to train a classifier and re-allocate the classes. But in the standard corrected images there was a level of variation that would lead to significant re-allocation of pixels between the NE and SW slopes based on shading. This is illustrated in Fig. 10(a) and (b) which shows how great the differences are between the slope categories in the uncorrected (standard) data relative to the terrain corrected data. In Fig. 10(b), the two cases for each class do not vary a great deal and the two classes have distinctive spectral signatures. The mean of the SW slopes for Class 3 shows the most deviation from equality after correction but must be interpreted carefully as there are relatively few pixels of Class 3 in the SW slopes stratum. In Fig. 10(a) there is a dramatic change. The range of variation in the two classes is similar to the differences in means which indicates that they are not statistically separable. Any subtle rainfall effect on vegetation, or variations due to annual radiation differences between northern and southern slopes, will be totally masked by this level of variation.

4.3.3. Comparison with CC, SCS and SCS + C methods

Fig. 10c, d and e also present the same plots for the images corrected using the CC, SCS and SCS + C methods. It is found that the degree of equalisation between the NE and SW slopes is almost the same as that of the physics-based method in most cases and that the resulting spectra are all very similar. The only correction method amongst these that had a relatively poor performance was the SCS method. This is consistent with the findings reported by Kane et al. (2008). On the other hand, the SCS + C method seems to have behaved a little better than the CC method if "better" is taken to mean greater equalisation between the slopes. As the CC and SCS + C methods estimate the irradiance effect statistically and empirically reduce the correlation between bands and the cosine of the incident angle, this reduction is to be expected. The uniformity of the outcomes is probably partly due to the simplicity of the Blue Mountains area where the structure of the vegetation cover was not disturbed over the time.

Quantitative comparisons are provided in Table 6. Table 6 summarises the reductions in the differences between means of same class in the NE and SW areas for the image of Apr. 15, 2006. It is based on the root mean square (RMS) difference between signatures from the same class but in the NE and SW sub-images in reflectance units. That is:

$$\text{RMS} = \left(\frac{1}{n_b} \sum_{j=1}^{n_b} \left(\rho_{\text{NE},j} - \rho_{\text{SW},j} \right)^2 \right)^{1/2} \quad (11)$$

In this measure, n_b is the number of spectral bands and the units are reflectance units. In Table 6, the results for the CC, Physics-based, SCS and SCS + C methods are presented as percentages of this RMS difference found for the Standard Product. The RMS for the standard product is provided unaltered in the last column. Using the percentages enables easier comparison between the first four methods. Class 5 is not shown as the numbers of pixels in this class within the NE and SW sub-images is small. As a guide to interpretation, smaller percent values for the

terrain correction methods are generally better. Overall, a value of 10–15% seems to represent an effective reduction with only the SCS method falling outside this range. The overall lowest set of reductions is found for the SCS + C method.

Since the classes were defined using a NDVI time series, it is expected that they will be spectrally similar between the NE and SW slopes after the application of any method and even in the standard corrected product. This turns out to be so in general but it is important to check whether any of the methods creates spectral changes. To provide some measures of this, Table 7 presents the same set of methods and classes as in Table 6 but the table now shows the RMS differences (multiplied by 100 for convenient percent scale) between NE and SW slopes when the mean reflectance values have been normalised so that they sum to 1.0 over the bands. This normalisation removes the brightness information and emphasises the spectral information. Large values indicate spectral differences. The results are presented for the four terrain correction products and also for the standard processed image on the same basis. If the column headed "Standard product" is taken as reference, Table 7 shows how the physics-based and empirical methods further reduce the spectral differences between the NE and SW slopes relative to the (already small) spectral differences between the NE and SW classes in the standard product. The SCS method does not change the spectral differences from those in the standard product. The two empirical methods reduce spectral differences by the greatest amount, but as in the cases of correlations, when the numbers are small the comparisons become more difficult. It seems that none of the correction methods distorts the spectral data.

5. Discussion

5.1. Physics-based models vs empirical models

The results here show how the physical model proposed in the paper, the CC model and SCS + C all gave good results with the test images. On the other hand, the SCS model without the advantage of the empirical C-correction did not perform well. The poorer results from SCS can be expected because the model does not include account for diffuse radiation and are consistent with results reported in Kane et al. (2008).

Previous studies (e.g. Richter et al., 2009; Soenen et al., 2005) show that if good estimates of the C coefficient in Eq. (8) can be obtained, the CC and SCS + C methods can provide good outcomes. Indeed, they have been used with success in the past, especially in cases where there is a single image to classify and there is insufficient information to apply atmospheric correction. Because of this, they have provided useful validation in the present paper for the proposed method. In the example reported here, C was obtained from atmospherically corrected reflectance images using cloud-free data. In addition, when Eq. (8) was developed, low relief and water covered areas were excluded using the DSM and the regression was obtained in areas of relatively uniform land cover. These conditions ensured that a stable value for C was obtained from the test images. However, in general applications, especially for an operational system, this situation is not always met. As Wu et al. (2004) observed, the requirements for representative training regions

Table 6
RMS differences between NE and SW means for each class.

	CC	Physics-based	SCS	SCS + C	Standard product (SP[a])
	% of SP	% of SP	% of SP	% of SP	SP NE and SW difference
Class 1	12.25	13.16	16.59	10.31	0.1236
Class 2	7.52	8.72	24.21	5.82	0.1163
Class 3	15.42	16.48	16.79	12.42	0.1178
Class 4	25.42	24.66	6.11	18.28	0.1222

[a] SP is in reflectance units.

Table 7
RMS (%) differences between normalised NE and SW means for each class.

	CC	Physics-based	SCS	SCS + C	Standard product
	RMS (%)	RMS (%)	RMS (%)	RMS (%)	RMS (%)
Class 1	0.71	1.09	2.71	0.69	2.61
Class 2	1.90	2.28	3.89	1.86	3.80
Class 3	2.20	2.55	4.20	2.15	4.02
Class 4	0.66	0.72	1.69	0.72	1.76

to estimate C can be difficult to meet, especially when cloud affects potential images so that there is not a sufficient number of terrain sample areas to derive a representative C. Wu et al. (2004) also pointed out that in more complex images, the estimated fitting parameters can change not only between different satellite scenes, but also between different areas within the same scene. This leads to the need for interactive evaluation of the model fit for each new image, or possibly different parts of the same image. Such a situation is operationally difficult to implement and consistency is harder to ensure than it is for a physics-based method. Since in an operational situation it is desirable for there to be as little empirical or data-dependent estimation of parameters as possible, this represents an advantage for the proposed physics-based approach.

The CC and SCS + C do not normally involve BRDF correction. This may create more significant difference in data from satellites with wider view angles and off-nadir pointing. As these methods do not normalise for the solar angle, there may also be inconsistencies in time series. A comparison using time series of data is needed to evaluate the performance of the different methods in these more complex situations. It is also not yet established from the limited studies reported here whether the empirical correction may sometimes remove useful information. For example, mountain areas may have directional effects that arise from environmental and slope related factors such as source of rainfall or solar radiation. These can lead to real differences in land cover that are hard to separate from shading effects and could be artificially balanced out by empirical modelling. The desirable outcome of the correction is to derive a time series of signatures such that if the land cover does not change then the signature will not change. Although it has not been proven that a time series from the proposed method can achieve this ideal, it seems that only a physics-based method will be able to achieve it.

5.2. DSM data

Effective resolution and high quality of DSM data are very important to ensure the accuracy of terrain correction and stability of the product. Topographic correction errors attributable to the DSM data include four main types. These are (i) error from the remaining DSM artefacts, (ii) error from mismatch between pixel coordinates of the DSM and Landsat images, (iii) error from resolution mismatch and (iv) error from within pixel DSM variation. Li et al (2011) have studied these sources of error and demonstrated how they can affect the accuracy of terrain corrected product, especially the mismatch between DSM and Landsat pixel coordinates. It was established that misregistration by one or two pixels can lead to significant errors in the gully and ridge areas. To ensure high quality in the terrain corrected product, accurate co-registration between satellite and DSM data, appropriate DSM spatial resolution and high quality DSM data are essential for the best results from terrain correction.

6. Conclusions

This paper presents a physics-based coupled BRDF and atmospheric correction model that can be applied to both flat and inclined surfaces. The algorithm has been shown to simultaneously reduce most of the BRDF, atmospheric and topographic effects at the scale of Landsat data. The algorithm has been tested in areas of Australia which have strong topographic effects by using eight Landsat scenes sensed at different seasons and solar zenith angles. Visual validation shows that the algorithm can remove most of the topographic effects and detect deep shadows in all cases. Indirect validation based on the correlation between the cosine of the incident angle and the surface reflectance factor shows that correlation is reduced significantly after the terrain correction algorithm has been applied. Most correlation coefficients after terrain correction are below 0.1 for band 4. The terrain corrected surface reflectance can also provide suitable input

data for multi-temporal land cover classification in areas of high relief and based on spectral signatures, which the standard product cannot.

The results were compared with CC, SCS and SCS + C methods. Although CC and SCS + C can also produce similarly good results for the 8 test images, the physics-based method proposed in this paper has significant advantages due to its capacity to apply the model anywhere and without using empirical adjustment or data-dependent interventions. The model can also be applied in extensively cloud affected images or these with complex terrain and land cover. This is particularly important in countries or regions where clear images are difficult to obtain, such as in East Asia and the pacific and other maritime tropical areas. The method combines atmospheric, BRDF and topographic correction, makes the three corrections together and it is designed to be especially convenient for use in an operational system. Since the product removes atmospheric, BRDF and topographic effects, it is well suited for time series analysis.

Appendix A. Atmospheric, BRDF and topographic correction algorithms

A.1. Solution for a horizontal surface

For a horizontal surface, if the semi-empirical BRDF kernel models and polynomial model for black and white sky albedo are used (Lucht et al., 2000), that is:

$$\rho_S(\theta_S, \theta_V, \delta\varphi) = F_{iso}\left(1 + \frac{F_{vol}}{F_{iso}}K_{vol} + \frac{F_{geo}}{F_{iso}}K_{geo}\right)$$
$$= F_{iso}B(\theta_S, \theta_V, \delta\varphi, \alpha1, \alpha2) \tag{a1}$$

$$\alpha_{bk}(1, \alpha1, \alpha2, \theta) = \overline{\rho}/F_{iso}$$
$$= 1 + \alpha1\left(-0.007574 - 0.070987\theta^2 + 0.307588\theta^3\right)$$
$$+ \alpha2\left(-1.284909 - 0.166314\theta^2 + 0.041840\theta^3\right) \tag{a2}$$

and $\alpha_{wk}(1, \alpha1, \alpha2) = \overline{\overline{\rho}}/F_{iso} = 1 + 0.189184\alpha1 - 1.377622\alpha2$ (a3)

where B ($\theta_S, \theta_V, \varphi, \alpha1, \alpha2$) is the BRDF shape function and α_{bk} and α_{wk} are its related black sky and white sky albedo derived from BRDF kernel models; F_{iso} is the isotropic contribution. F_{vol} and F_{geo} are the weights for volume-scattering and geometric-optical contributions and K_{vol} and K_{geo} are volume-scattering and geometrical-optical scatting kernel functions. K_{vol} and K_{geo} are defined functions of θ_S, θ_V and $\delta\varphi$. Here, $\alpha1$ and $\alpha2$ are defined as: $\alpha1 = F_{vol}/F_{iso}$ and $\alpha2 = F_{geo}/F_{iso}$.

In this situation, Eq. (1) in the paper can be solved as a quadratic equation (Li et al., 2010):

$$(1-a)S(1-S\rho_m)\overline{\overline{\rho}}^2 + [a + \rho_m(1-a)S]\overline{\overline{\rho}} - \rho_m = 0 \tag{a4}$$

where f_V and f_S are defined as:$f_V = t_V/(t_V + t_d(\theta_V)) = t_V/T_V$ and $f_S = t_S/(t_S + t_d(\theta_S)) = t_S/T_S$ and a is defined as:

$$
\begin{aligned}
a = 1/\alpha_{wk}(1,\alpha1,\alpha2)[&f_V f_S B(\theta_S,\theta_V,\delta\varphi,\alpha1,\alpha2) \\
&+ f_V(1-f_S)\alpha_{bk}(1,\alpha1,\alpha2,\theta_V) + f_S(1-f_V)\alpha_{bk}(1,\alpha1,\alpha2,\theta_S) \\
&+ (1-f_S)(1-f_V)\alpha_{wk}(1,\alpha1,\alpha2)]
\end{aligned}
$$

A.2. Atmospheric and BRDF correction for an inclined surface

According to the definition of E_h, E_h^{dir}, E_h^{dif}, t_S, $t_d(\theta_S)$ and T_S in Table 1, the irradiance components can be expressed as:

$$
E_h^{dir} = t_S E'_0 \cos(\theta_S), E_h^{dif} = t_d(\theta_S)E'_0 \cos(\theta_S) \text{ and } E_h = E_h^{dir} + E_h^{dif} = T_S E'_0 \cos(\theta_S)
$$

Thus f_S can also be expressed as:

$$
f_S = t_S/T_S = E_h^{dir}/E_h \text{ and } 1-f_S = t_d(\theta_S)/T_S = E_h^{dif}/E_h
$$

In this notation, Eq. (1) can be rewritten:

$$
L_{TOA} = L_0 + \frac{T_V}{\pi}\left(\begin{array}{l} E_h^{dir}\left[f_V\rho_S(\theta_S,\theta_V,\delta\varphi) + (1-f_V)\overline{\rho'}\right] + \\ E_h^{dif}\left[f_V\overline{\rho} + (1-f_V)\overline{\overline{\rho}}\right] + E_h\dfrac{S\overline{\overline{\rho}}^2}{1-S\overline{\overline{\rho}}}\end{array}\right) \tag{a5}
$$

In a similar way to the horizontal surface, Eq. (a5) for an inclined surface can be expressed as:

$$
L_{TOA} = L_0 + \frac{T_V}{\pi}\left(\begin{array}{l} E^{dir}\left[f_V\rho_S(i_t,e_t,\delta\varphi_t) + (1-f_V)\overline{\rho'}(i_t)\right] + \\ E^{dif}\left[f_V\overline{\rho}(e_t) + (1-f_V)\overline{\overline{\rho}}\right] + E\dfrac{S\left(\overline{\overline{\rho}}\right)^2}{1-S\overline{\overline{\rho}}}\end{array}\right) \tag{a6}
$$

where $\delta\varphi_t$ is the relative azimuth angle between incident and exiting directions in the slope geometry and $\delta\varphi_t = |\varphi_i - \varphi_e|$. Other terms were defined in Table 1. Eq. (a6) assumes that the BRDF for an inclined surface is taken to be equivalent to the BRDF for the horizontal surface but with modified source, view and relative azimuthal angles.

Parameters i_t, e_t, φ_i, and φ_e can be calculated as (Pearson, 1990):

$$
\cos(i_t) = \cos(\theta_S)\cos(\theta_t) + \sin(\theta_S)\sin(\theta_t)\cos(\varphi_S - \varphi_t) \tag{a7}
$$

$$
\cos(e_t) = \cos(\theta_V)\cos(\theta_t) + \sin(\theta_V)\sin(\theta_t)\cos(\varphi_V - \varphi_t) \tag{a8}
$$

$$
\tan(\varphi_i) = \frac{\sin(\theta_S)\sin(\varphi_S - \varphi_t)}{\cos(\theta_S)\sin(\theta_t) - \sin(\theta_S)\cos(\theta_t)\cos(\varphi_S - \varphi_t)} \tag{a9}
$$

$$
\tan(\varphi_e) = \frac{\sin(\theta_V)\sin(\varphi_V - \varphi_t)}{\cos(\theta_V)\sin(\theta_t) - \sin(\theta_V)\cos(\theta_t)\cos(\varphi_V - \varphi_t)} \tag{a10}
$$

θ_t, φ_t, φ_S and φ_V are defined in Table 1 and the inter-relationships between them are shown diagrammatically in Fig. 1.

The total irradiance is the sum of E^{dir} and E^{dif}. According to Iqbal (1983) and Shepherd and Dymond (2003), E^{dir} can be estimated as:

$$
E^{dir} = E_h^{dir}\Theta\frac{\max(\cos(i_t),0)}{\cos(\theta_S)} \tag{a11}
$$

In this expression, Θ is a binary coefficient, set to zero in cast shadow (shadow due to obstruction by other parts of the terrain) and set to one otherwise.

For the diffuse radiation,

$$
E^{dif} = E^{sky} + E^{adj} \tag{a12}
$$

where E^{sky} is sky diffuse radiation incident on an inclined surface and E^{adj} is ground-reflected radiation incident on an inclined plane (Iqbal, 1983),

For a Lambertian surface, E^{sky} and E^{adj} can be calculated as:

$$
E^{sky} = E_h^{dif}V_d \text{ and } E^{adj} = E_hV_t\rho_{adj} \tag{a13}
$$

With the diffuse view factor $V_d = [1 + \cos(\theta_t)]/2$
And the terrain view factor $V_t = [1 - \cos(\theta_t)]/2 = 1 - V_d$
Other terms are defined in Table 1.

For anisotropic surfaces, Klucher (1979) modified Temps and Coulson (1977) model and suggested that E^{sky} and E^{adj} can be calculated as:

$$
E^{sky} = E_h^{dif}V_d\left[1 + f_S\sin^3(\theta_t/2)\right]\left[1 + f_S\cos^2(i_t)\sin^3(\theta_S)\right] = E_h^{dif}F_d \tag{a14}
$$

and $E^{adj} = E_hV_t\rho_{adj}\left[1 + \sin^2(\theta_S/2)\right][|\cos\Delta|] = E_h\rho_{adj}F_t$ (a15)

where Δ is the azimuth of the inclined surface with respect to that of the sun (Iqbal, 1983).

Define $R^{dir} = E^{dir}/E_h$, $R^{dif} = E^{dif}/E_h$ and $R = E/E_h$ and defining the horizontal Lambertian solution (ρ_m) in Eq. (2), Eq. (a6) can then be expressed as:

$$
\frac{\rho_m}{1-S\rho_m} = \left(\begin{array}{l} R^{dir}\left[f_V\rho_S(i_t,e_t,\delta\varphi_t) + (1-f_V)\overline{\rho'}(i_t)\right] + \\ R^{dif}\left[f_V\overline{\rho}(e_t) + (1-f_V)\overline{\overline{\rho}}\right] + R\dfrac{S\left(\overline{\overline{\rho}}\right)^2}{1-S\overline{\overline{\rho}}}\end{array}\right) \tag{a16}
$$

In a similar way to the horizontal case, Eq. (a16) can be solved using a quadratic equation:

$$
(R-a_t)S(1-S\rho_m)\overline{\overline{\rho}}^2 + [a_t + \rho_m(1-a_t)S]\overline{\overline{\rho}} - \rho_m = 0 \tag{a17}
$$

with

$$
\begin{aligned}
a_t = 1/\alpha_{wk}(1,\alpha1,\alpha2)\{&R^{dir}[f_VB(i_t,e_t,\delta\varphi_t,\alpha1,\alpha2) \\
&+ (1-f_V)\alpha_{bk}(1,\alpha1,\alpha2,i_t)] + R^{dif}[f_V\alpha_{bk}(1,\alpha1,\alpha2,e_t) \\
&+ (1-f_V)\alpha_{wk}(1,\alpha1,\alpha2)]\}
\end{aligned}
$$

where B (i_t, i_e, $\delta\varphi_t$, $\alpha1$, $\alpha2$) is BRDF shape functions on the inclined surface geometry and α_{bk} and α_{wk} are its related black sky and white sky albedo.

References

Dozier, J., Bruno, J., & Downey, P. (1981). A faster solution to the horizon problem. *Computers & Geosciences, 7*, 145–151.

Dozier, J., & Frew, J. (1981). Atmospheric corrections to satellite radiometric data over rugged terrain. *Remote Sensing of Environment, 11*, 191–205.

Dozier, J., & Frew, J. (1990). Rapid calculation of terrain parameters for radiation modeling from digital elevation data. *IEEE Transactions on Geoscience and Remote Sensing, 28*, 963–969.

Dymond, J. R., Shepherd, J. D., & Qi, J. (2001). A simple physical model of vegetation reflectance for standardising optical satellite imagery. *Remote Sensing of Environment, 77*, 230–239.

Geoscience Australia and CSIRO Land & Water (2010). 1 Second SRTM Derived Digital Elevation Models User Guide. Version 1.0. Geoscience Australia. http://www.ga.gov.au/image_cache/GA18067.pdf

Giles, P. (2001). Remote sensing and cast shadows in mountainous terrain. *Photogrammetric Engineering and Remote Sensing, 67*, 833–839.

Gu, D., & Gillespie, A. (1998). Topographic normalization of landsat TM images of forest based on subpixel sun-canopy-sensor geometry. *Remote Sensing of Environment, 64*, 166–175.

Hapke, B. (1981). Bidirectional reflectance spectroscopy, 1, Theory. *Journal of Geophysical Research, 86*, 3039–3054.

Hu, B., Lucht, W., & Strahler, A. (1999). The interrelationship of atmospheric correction of reflectances and surface BRDF retrieval: a sensitivity study. *IEEE Transactions on Geoscience and Remote Sensing, 37*, 724–738.

Iqbal, M. (1983). *An introduction to solar radiation* (pp. 390). New York: Academic.

Kalnay, E., Kanamitsu, M., Kistler, R., Collins, W., Deaven, D., Gandin, L., et al. (1996). The NCEP/NCAR 40-Year Reanalysis Project. *Bulletin of the American Meteorological Society, 77*, 437–471.

Kane, V. R., Gillespie, A. R., McGaughey, R., Lutz, J. A., Ceder, K., & Franklin, J. F. (2008). Interpretation and topographic compensation of conifer canopy self-shadowing. *Remote Sensing of Environment*, *112*, 3820–3832.

Klucher, T. M. (1979). Evaluation of models to predict insolation on tilted surfaces. *Solar Energy*, *23*, 111–114.

Kriegler, F. J., Malila, W. A., Nalepka, R. F., & Richardson, W. (1969). Preprocessing transformations and their effects on multispectral recognition. *Proc. 6th Int. Symp. On Remote Sensing of Environment* (pp. 97–109). Ann Arbor, MI: ERIM.

Li, F., Jupp, D. L. B., Reddy, S., Lymburner, L., Mueller, N., Tan, P., et al. (2010). An evaluation of the use of atmospheric and BRDF correction to standardize Landsat data. *The IEEE Journal of Selected Topics in Applied Earth Observations and Remote Sensing*, *3*, 257–270.

Li, F., Jupp, D. L. B., & Thankappan, M. (2011). Using high resolution DSM data to correct the terrain illumination effect in Landsat data. *19th International Congress on Modelling and Simulation, Perth, Australia, 12–16 December 2011*.

Li, X., & Strahler, A. H. (1985). Geometric-optical modeling of a conifer forest canopy. *IEEE Transactions on Geoscience and Remote Sensing, GE-23*, 705–721.

Li, X., Strahler, A. H., & Woodcock, C. E. (1995). A hybrid geometric optical radiative transfer approach for modeling albedo and directional reflectance of discontinuous canopies. *IEEE Transactions on Geoscience and Remote Sensing*, *33*, 466–480.

Liang, S. (2004). *Quantitative Remote Sensing of Land Surface.* : Wiley-Interscience 534 pp.

Lucht, W., Schaaf, C., & Strahler, A. (2000). An algorithm for the retrieval of albedo from space using semiempirical BRDF models. *IEEE Transactions on Geoscience and Remote Sensing*, *38*, 977–998.

Pearson, F. (1990). *Map projections: Theory and applications* (pp. 372). London: CRC.

Richter, R. (1997). Correction of atmospheric and topographic effects for high spatial resolution satellite imagery. *International Journal of Remote Sensing*, *18*, 51099–51111.

Richter, R., Kellenberger, T., & Kaufmann, H. (2009). Comparison of topographic correction methods. *Remote Sensing*, *1*, 184–196.

Schaaf, C., Gao, F., Strahler, A. H., Lucht, W., Li, X., Tsang, T., et al. (2002). First operational BRDF, albedo and nadir reflectance products from MODIS. *Remote Sensing of Environment*, *83*, 135–148.

Schaaf, C. B., Li, X., & Strahler, A. H. (1994). Topographic effects on bidirectional and hemispherical reflectances calculated with a geometric-optical canopy model. *IEEE Transactions on Geoscience and Remote Sensing*, *32*, 1186–1193.

Shepherd, J. D., & Dymond, J. R. (2003). Correcting satellite imagery for the variance of reflectance and illumination with topography. *International Journal of Remote Sensing*, *24*, 3503–3514.

Smith, J. A., Lin, T. L., & Ranson, K. J. (1980). The Lambertian assumption and Landsat data. *Photogrammetric Engineering and Remote Sensing*, *46*, 1183–1189.

Soenen, S. A., Peddle, D. R., & Coburn, C. A. (2005). SCS+C: A modified sun-canopy-sensor topographic correction in forested terrain. *IEEE Transactions on Geoscience and Remote Sensing*, *43*, 2148–2159.

Teillet, P. M., Guindon, B., & Goodenough, D. G. (1982). On the slope-aspect correction of multispectral scanner data. *Canadian Journal of Remote Sensing*, *8*, 84–106.

Temps, R. C., & Coulson, K. L. (1977). Solar radiation incident upon slopes of different orientations. *Solar Energy*, *19*, 179–184.

Vermote, E., Saleous, N. El, Justice, C. O., Kaufman, Y. J., Privette, J., Remer, L., et al. (1997). Atmospheric correction of visible to middle-infrared EOS-MODIS data over land surfaces: Background, operational algorithm and validation. *Journal of Geophysical Research*, *102*(D14), 17131–17141.

Wang, S., Haralick, R. M., & Campbell, J. (1984). Relative elevation determination from Landsat imagery. *Photogrammetrica*, *39*, 193–215.

Wen, J., Liu, Q., Liu, Q., Xiao, Q., & Li, X. (2009). Parametrized BRDF for atmospheric and topographic correction and albedo estimation in Jiangxi rugged terrain, China. *International Journal of Remote Sensing*, *30*, 112875–112896.

Wu, X., Furby, S., & Wallace, J. (2004). An approach for terrain illumination correction. *The 12th Australasian Remote Sensing conference, Fremantle, WA*.